Microchemical Journal 126 (2016) 287–295

Contents lists available at ScienceDirect

Microchemical Journal

journal homepage: www.elsevier.com/locate/microc

Improvements in the PIGE technique via gamma-ray angular distribution☆

Paula Rangel Pestana Allegro *, Márcia de Almeida Rizzutto, Nilberto Heder Medina

Institute of Physics, University of São Paulo, 05508-090 São Paulo, São Paulo, Brazil

ARTICLE INFO

Article history:
Received 15 August 2015
Received in revised form 7 December 2015
Accepted 7 December 2015
Available online 15 December 2015

Keywords:
PIGE
Gamma-ray angular distribution
Material analysis

ABSTRACT

Particle induced gamma-ray emission (PIGE) is an ion beam technique used for isotopic elemental analysis of materials, based on gamma-ray spectroscopy. In the traditional PIGE setup, the gamma-ray detector is positioned at the neutral angles 55° or 125° with respect to the beam direction in order to measure gamma-rays with different angular distributions. Although these angles permit measurements without an a-priori knowledge of the specific angular distributions, this choice is not efficient if one wants to identify a specific element since a longer acquisition time is needed.

In this work, we propose to optimize the PIGE measurements by choosing the detector angle position due to the previous knowledge of the gamma-ray multipolarity and the nuclear reaction. We present the angular distribution calculations for the isotopes most frequently identified by PIGE analysis, specially in Cultural Heritage objects. Calculations demonstrate that a gain in the intensity up to 70% can be achieved allowing the elemental identification in shorter times. This result is promising and represents a more efficient alternative to perform PIGE measurements.

1. Introduction

Particle induced gamma-ray emission (PIGE) [1,2] is an ion beam technique based on gamma-ray spectroscopy largely employed to determine elemental composition in a wide variety of materials. For example, it is currently applied to study aerosol samples [3], teeth dentin [4], medicinal plants [5], welded steel joints [6], minerals [7] and Cultural Heritage objects, such as ceramic artifacts [8], glasses [9] and paintings [10]. In most cases, PIGE is commonly used to identify a specific element in a study matrix like fluorine distribution in teeth, oxygen and carbon in steel joints, and sodium in blue pigments made of lapis-lazuli.

Ion beam analysis techniques are based on accelerated charged particles colliding with atoms and nuclei and several reactions can take place simultaneously during the beam-target interaction. The elemental identification depends on several factors such as the beam intensity, beam energy, reaction cross-section, and number of atoms in the sample. In particular, in PIGE technique inelastic nuclear reactions with light nucleus beams (protons, deuterons and alpha particles) are used to excite the nuclei in the sample, but fusion reactions occur as well in the process, resulting in the production of new excited nuclei. In general, the excited nuclei decay emitting characteristic gamma-rays with well known energies which can be used to determine the elemental composition of the sample. In some fusion reactions, it is possible to produce a new isotope which β^- decays to an excited state of another nucleus with atomic number Z-1 that will also decay via gamma-ray emission. The gamma-ray intensities can be used to determine the elemental concentration at a larger depth inside a sample [11], since high energy gamma-rays (100 keV to 10 MeV) are slightly attenuated inside the material compared to the totally absorbed low energy X-rays (from hundreds of eV to tens of keV).

PIGE is usually performed in small accelerators with protons, alpha particles and/or deuteron beams [12–14]. The use of low energies to accelerate the beam projectiles (typically 2–3 MeV for protons) restricts the quantity of reactions that can be performed due to the Coulombian repulsion between the beam and target nuclei. This fact restricts the elements that can be analyzed by this technique, consequently, PIGE is mostly used to identify and to quantify light elements such as Li, Be, B, C, O, F, Na, Mg, Al, Si and P, not easily detected by other ion beam techniques, such as particle induced X-ray emission (PIXE). However, PIGE can be used to detect heavier elements with appropriate nuclear reactions.

PIGE detection limits vary greatly from isotope to isotope because it is based upon specific nuclear reactions, and typical values are between 10 and 100 ppm. To achieve those detection limits, it is necessary to take into account that nuclear reaction cross-sections are small (ranging from few mbarns to hundreds of mbarns) and also to consider the particularities of the gamma-ray emission and its detection efficiency (typically 10^{-3}–10^{-5} full-energy peak absolute efficiency for a HPGe

☆ Selected papers presented at TECHNART 2015 Conference, Catania (Italy), April 27–30, 2015.

* Corresponding author.
E-mail addresses: allegro@if.usp.br (P.R.P. Allegro), rizzutto@if.usp.br (M.A. Rizzutto), medina@if.usp.br (N.H. Medina).

http://dx.doi.org/10.1016/j.microc.2015.12.012
0026-265X/

gamma-ray detector). These factors contribute to the increasing of the measurement time and the beam exposure required to have enough data to perform a quantitative analysis. In some cases, however, the increase of the beam exposure raises the chance of radiation damage in the sample even when using an external beam, a specially unwanted effect in the study of Cultural Heritage objects such as paintings [15–17] and ceramics [18].

The gamma-ray emission properties play an important role in the position of the gamma-ray detector and in the beam time exposure. We know from gamma-ray spectroscopy that excited states produced in nuclear reactions generally have an oriented angular distribution which depends on the nuclear reaction type to populate the excited states and on the emitted gamma-ray multipolarities [19]. To minimize the contribution of the angular distribution in the quantitative results, a traditional PIGE setup places the gamma-ray detector at 55° or 125° with respect to the beam direction [20]. Although these positions permit to measure gamma-rays with different angular distributions, they do not detect the maximum of the emission, increasing the beam time exposure. This setup, however, is the best option when the electromagnetic properties of the transition are unknown or when the measurement of simultaneous gamma-rays with different multipolarities is required.

With all this in mind, we propose to optimize the PIGE technique in the cases where a specific element is under study by changing the detector angle position based on the previous knowledge of the gamma-ray angular distributions. With this approach, it is possible to detect the maximum of the gamma emission and consequently minimize the measurement time and the radiation dose applied to the sample, which is very important in the case of Cultural Heritage objects. In this work we present the angular distribution calculations for the isotopes most frequently identified by PIGE technique based on the previous knowledge of the isotope nuclear structure provided by gamma-ray spectroscopy studies.

2. Angular distribution theory overview

The angular distribution can be classified by the shape of the orientation with respect to the quantization axis as non-orientation, polarization and alignment [19]. The non-orientation is defined when there is no preferential orientation, an example is the gamma-ray emission of a radioactive source. Polarization is defined when there is a preferential direction of the gamma-ray emission, like the thermal equilibrium orientation realized by Zeeman effect at low temperatures. Alignment occurs when there is an orientation regarding to a quantization axis. The degree of orientation depends on the state formation process and is closely related with the reaction mechanisms. Nuclear reactions or gamma–gamma angular correlations are processes conserving the parity of the states, consequently, only alignment is realized in such processes [19].

Several reaction mechanisms can occur with different probabilities during the interaction of the beam projectiles with the sample depending on the beam's energy and on the type of accelerated particle. As a result, a state with angular momentum j and a projection m along the quantization axis (the direction of the beam projectiles in a nuclear reaction) can be populated with a probability depending on the nuclear reaction type. To solve this problem, we are going to deal with an assembly of systems composed of pure states with probability $P(m)$ to be oriented with respect to a suitable symmetry axis as the quantization axis, which can be described by the statistical tensor $\rho_k(j)$ (1):

$$\rho_k(j) = \sqrt{2j+1}\sum_m (-1)^{j-m}\langle \mathrm{jmj}-m|k0\rangle P(m) \qquad k = 0, 1, \ldots 2j. \tag{1}$$

The angular distribution is also dependent on the gamma-ray multipole radiation and the mixture between them. This multipole radiation is closely connected to electromagnetic properties of nuclear states and can be classified as 2^{λ}-pole charge ($E\lambda$) or magnetization ($M\lambda$) distribution. The degree of mixture between electric and magnetic radiation is given by the mixing ratio δ, defined as $\delta = \langle j_f \| \lambda' \| j_i\rangle / \langle j_f \| \lambda \| j_i\rangle$. In this work, we follow the δ signal convention of Krane and Steffen [21], in accordance with the used in the nuclear data sheet tables [22].

The gamma-ray angular distribution $W(\theta)$ [19] from an oriented state is expressed as follows,

$$W(\theta) = \sum_k^{k_{\max}} A_k\left(j_i \lambda \lambda' j_f\right) P_k(\cos\theta) \qquad k_{\max} = \min\{2j_i,\ \max\{2\lambda, 2\lambda'\}\} \tag{2}$$

$$A_k\left(j_i\lambda\lambda' j_f\right) = \rho_k(j_i)\frac{1}{1+\delta^2}\left[F_k\left(j_f\lambda\lambda j_i\right) + 2\delta F_k\left(j_f\lambda\lambda' j_i\right) + \delta^2 F_k\left(j_f\lambda'\lambda' j_i\right)\right] \tag{3}$$

$$F_k\left(j_f\lambda\lambda' j_i\right) = (-1)^{1+j_i-j_f}\sqrt{(2j_i+1)(2\lambda+1)(2\lambda'+1)} \times \langle \lambda 1 \lambda' -1|k0\rangle W\left(j_i j_i \lambda\lambda'; k j_f\right) \tag{4}$$

where $P_k(\cos\theta)$ is the Legendre polynomial; j_i and j_f are the spins of the initial and final states; λ and λ' are the multipole order of the radiation; δ is the mixing ratio of the electromagnetic transition; $W(j_i j_i \lambda\lambda'; k j_f)$ are the six-symbol Racah coefficients and $\rho_k(j_i)$ is the statistical tensor given by Eq. (1).

Eq. (2) is normalized to take into account an isotropic angular distribution ($k = 0$), so the quantities $A_0(j_i\lambda\lambda' j_f)$ and $P_0(\cos\theta)$ are equal to 1. $W(\theta)$ describes the gamma-ray intensities dependency with the observation angle and usually varies between 0 and 2.

An isotropic angular distribution happens in the special cases of $j = 0$ and $j = 1/2$ as can be seen from Eq. (2), since for $j = 0$ no orientation exists and a $j = 1/2$ state has only two substates $m = \pm 1/2$. In general, an aligned oriented state with population parameters $P(m)$ has the same statistical tensor $\rho_k(j)$ for even k as the inversely oriented state with population parameters $P(m) = P(-m)$. Therefore the angular distribution for both states is equal due to the invariance under space inversion.

It is possible to have a total or partial alignment of the nuclear substates m. In total oblate alignment, $\rho_2(j) < 0$ and the population of the substates are $P(m = 0) = 1$ or $P(m = \pm 1/2) = 1$ while in the total prolate alignment, $\rho_2(j) > 0$ and $P(m = \pm j) = 1$. In the case of a partial alignment, the population of the substates m can be approximated by a Gaussian [23] given by:

$$P(m) = \frac{\exp(-c^2/2\sigma^2)}{\sum_{m'=-j}^{j}\exp\left(-m'^2/2\sigma^2\right)} \tag{5}$$

where $c = m$ for oblate alignment and $c = j - |m|$ for prolate alignment; σ is the Gaussian width, usually described as a $\sigma = constant^* j$.

The case $\sigma \to 0$ corresponds to complete alignment while the value for σ in the partial alignment depends mainly on the nuclear reaction type and on the incident beam energy. To determine if a state is totally aligned in indirect reactions, it is necessary to position a particle detector near 180° and perform a coincidence method and correct the angular distribution due to correlations [24]. If a particle is detected in this angle, in coincidence with the gamma-ray, the substate m populated is the one from the total alignment.

3. Results and discussion

A routine to calculate $W(\theta)$ was developed using MATLAB® [25] to consider different nuclei input parameters such as the initial (j_i) and final (j_f) state spins, the transition multipolarities and subsequently the transition mixing ratio (δ). In the mixed transitions, the experimental δ was used when known and the experimental error of this value was

ignored in the calculations. The numerical error in the calculated results is of order of 10^{-12}. It is important to consider that the experimental error in the gamma-ray intensity obtained in an angular distribution measurement will be due to the experimental factors, as the detector position and efficiency, measured δ values, number of nuclei in the sample, etc. The calculations were also performed considering a defined angular position of the detector, but the conclusions are still valid considering the total detector opening angle since an integration of the intensities is needed to take into account the radiation measured by the detector.

The results obtained from Eq. (2) are independent on the gamma-ray energies, but they are strongly dependent on the gamma-ray multipolarities including mixing ratios, on the initial and final state spins and also on the population of the substates m of the initial state. Also, the results are valid for the use of detectors in single acquisition mode. In the case of using a coincidence method, it is also necessary to calculate the angular correlation between the emitted gamma-rays, a fact that will change the gamma-ray angular distribution seen by the detectors due to the introduction of another preferential axis. More details about this procedure can be found in Ref. [24].

Table 1 presents the principal gamma-rays and nuclear reactions used to produce the nuclei interest in PIGE technique. This table resumes all the informations necessary to identify the nuclei, such as the most common nuclear reaction, the most used gamma-rays to be detected and it also indicates the graph number of the angular distribution presented in the subsections below. In the following the gamma-ray energies will be shown together with their uncertainty, within brackets.

3.1. The ^{19}F nuclei

The angular distribution of the most commonly identified gamma-rays from the excited ^{19}F nucleus is shown in Fig. 1. As discussed in Section 2, initial states with $j_i = 1/2$ or 0 emit gamma-rays with an isotropic distribution, as seen in Fig. 1(a) for the ^{19}F 109.9 (2) keV gamma-ray transition from $j_i^\pi = 1/2^-$ to $j_f^\pi = 1/2^+$ state. The measurement is independent on the angle where the detector is positioned since a $j_i = 1/2$ state has only two substates $m = \pm 1/2$. The distribution is therefore flat.

Fig. 1(b) and (c) shows the angular distribution of the 197.1 (2) keV and 1235.8 (5) keV pure E2 transitions, respectively. Both have the same angular distribution since they come from a $j_i = 5/2$ state and since the angular distribution is independent on the parity of the nuclear state, as can be seen in Eq. (2). For a pure E2 transition from a $j_i = 5/2$ state, the gain in the gamma-ray intensity after changing the detection angle to 45° instead of 55° is 13% for total oblate alignment of the nuclear substates and 12% for partial oblate alignment of the nuclear

Table 1
Some studied sample nuclei by using PIGE technique. The typical reactions used to study the nuclei present in the sample were taken from [20], the isotopic abundances were taken from [26], while the detected gamma-ray properties, such as energies (E_γ), multipolarities and mixing ratio (δ) and also the initial (j_i) and final (j_f) state spins were taken from literature (see Ref. column). The column labeled Figure made reference to the angular distribution graph numbers for each gamma-ray, also presented in this article. All uncertainties are given within brackets.

Sample nuclei	Abundance (%) [26]	Typical reaction [20]	Measured nuclei	E_γ (keV)	j_i	j_f	Multipolarity	δ	Ref.	Figure
^{19}F	100	$^{19}F(p,p'\gamma)^{19}F$	^{19}F	109.9 (2)	$1/2^-$	$1/2^+$	E1	–	[27]	1(a)
				197.1 (2)	$5/2^+$	$1/2^+$	E2	–	[27]	1(b)
				1235.8 (5)	$5/2^-$	$1/2^-$	E2	–	[27]	1(c)
				2582.7 (5)	$9/2^+$	$5/2^+$	E2	–	[27]	1(d)
^{23}Na	100	$^{23}Na(p,p'\gamma)^{23}Na$	^{23}Na	439.986 (10)	$5/2^+$	$3/2^+$	M1 + E2	+0.058 (3)	[28]	3(a)
				1635.96 (3)	$7/2^+$	$5/2^+$	M1 + E2	+0.19 (1)	[28]	3(b)
				627.48 (4)	$9/2^+$	$7/2^+$	M1 + E2	+0.10 (2)	[28]	3(c)
				2263.39 (3)	$9/2^+$	$5/2^+$	E2 + (M3)	−0.01 (3)	[28]	3(d)
		$^{23}Na(p,\gamma)^{24}Mg$	^{24}Mg	1368.626 (5)	2^+	0^+	E2	–	[29]	4(a)
				2754.007 (11)	4^+	2^+	E2	–	[29]	4(b)
		$^{23}Na(p,\alpha\gamma)^{20}Ne$	^{20}Ne	1633.602 (15)	2^+	0^+	E2	–	[30]	2(a)
				2613.8 (11)	4^+	2^+	E2	–	[30]	2(b)
^{24}Mg	78.99 (4)	$^{24}Mg(p,p'\gamma)^{24}Mg$	^{24}Mg	1368.626 (5)	2^+	0^+	E2	–	[29]	4(a)
				2754.007 (11)	4^+	2^+	E2	–	[29]	4(b)
^{25}Mg	10.00 (1)	$^{25}Mg(p,p'\gamma)^{25}Mg$	^{25}Mg	585.028 (30)	$1/2^+$	$5/2^+$	E2	–	[31]	5(a)
				389.710 (35)	$1/2^+$	$3/2^+$	M1 + E2	+0.13 (3)	[31]	5(b)
				974.742 (35)	$3/2^+$	$5/2^+$	M1 + E2	+0.36 (2)	[31]	5(c)
^{26}Mg	11.01 (3)	$^{26}Mg(p,p'\gamma)^{26}Mg$	^{26}Mg	1808.66 (3)	2^+	0^+	E2	–	[32]	6(a)
				1129.58 (5)	2^+	2^+	M1 + E2	−0.12 (2)	[32]	6(b)
				2510.02 (7)	4^+	2^+	E2	–	[32]	6(c)
		$^{26}Mg(p,\gamma)^{27}Al$	^{27}Al	843.76 (10)	$1/2^+$	$5/2^+$	E2	–	[33]	7(a)
				1014.52 (10)	$3/2^+$	$5/2^+$	M1 + E2	−0.351 (12)	[33]	7(b)
^{27}Al	100	$^{27}Al(p,p'\gamma)^{27}Al$	^{27}Al	843.76 (10)	$1/2^+$	$5/2^+$	E2	–	[33]	7(a)
				1014.52 (10)	$3/2^+$	$5/2^+$	M1 + E2	−0.351 (12)	[33]	7(b)
				2212.01 (10)	$(7/2^+)$	$5/2^+$	M1 + E2	+0.468 (9)	[33]	7(c)
		$^{27}Al(p,\gamma)^{28}Si$	^{28}Si	1778.969 (11)	2^+	0^+	E2	–	[34]	8(a)
				2838.29 (15)	$3/2^+$	$5/2^+$	M1 + E2	−0.351 (12)	[34]	8(b)
		$^{27}Al(p,\alpha\gamma)^{24}Mg$	^{24}Mg	1368.626 (5)	2^+	0^+	E2	–	[29]	4(a)
^{28}Si	92.223 (19)	$^{28}Si(p,p'\gamma)^{28}Si$	^{28}Si	1778.969 (11)	2^+	0^+	E2	–	[34]	8(a)
				2838.29 (15)	4^+	2^+	E2	–	[34]	8(b)
^{29}Si	4.685 (8)	$^{29}Si(p,p'\gamma)^{29}Si$	^{29}Si	1273.361 (9)	$3/2^+$	$1/2^+$	M1 + E2	+0.197 (9)	[35]	9(a)
				1793.83 (8)	$5/2^+$	$3/2^+$	M1 + E2	+0.26 (2)	[35]	9(b)
^{30}Si	3.092 (11)	$^{30}Si(p,p'\gamma)^{30}Si$	^{30}Si	1263.13 (3)	2^+	2^+	M1 + E2	+0.18 (5)	[36]	10(a)
				2235.23 (2)	2^+	0^+	E2	–	[36]	10(b)
				3498.33 (5)	2^+	0^+	E2	–	[36]	10c)
				3043.2 (1)	4^+	2^+	E2	–	[36]	10(d)
		$^{30}Si(p,\gamma)^{31}P$	^{31}P	1266.1 (1)	$3/2^+$	$1/2^+$	M1 + E2	+0.28 (2)	[37]	11(a)
				2028.8 (2)	$5/2^+$	$3/2^+$	M1 + E2	+0.44 (2)	[37]	11(b)
^{31}P	100	$^{31}P(p,p'\gamma)^{31}P$	^{31}P	1266.1 (1)	$3/2^+$	$1/2^+$	M1 + E2	+0.28 (2)	[37]	10(a)
				2028.8 (2)	$5/2^+$	$3/2^+$	M1 + E2	+0.44 (2)	[37]	11(b)
		$^{31}P(p,\alpha\gamma)^{28}Si$	^{28}Si	1778.969 (11)	2^+	0^+	E2	–	[34]	8(a)

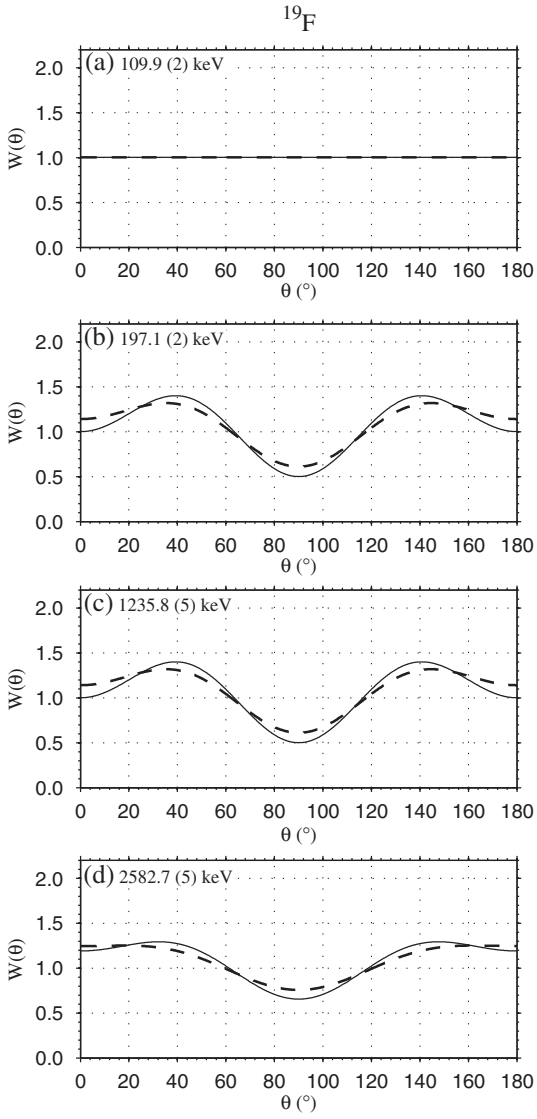

Fig. 1. Angular distribution ($W(\theta)$) of ^{19}F gamma-rays: (a) 109.9 (2) keV, (b) 197.1 (2) keV, (c) 1235.8 (5) keV and (d) 2582.7 (5) keV. In this figure, the solid line is the angular distribution considering total oblate alignment of the nuclear substates while the dashed line is the angular distribution considering partial oblate alignment of the nuclear substates with $\sigma/J = 0.3$.

substates with $\sigma/J = 0.3$. The 2582.7 (5) keV gamma-ray is also a pure E2 transition, but its angular distribution (see Fig. 1(d)) is flatter than the angular distribution of the 197.1 (2) and 1235.8 (5) keV gamma-rays. So, in this case (pure E2 transition from a $j_i = 9/2$ state), the gain in the gamma-ray intensity after changing the detection angle to 45° instead of 55° is 12% for total oblate alignment of the nuclear substates and 9% for partial oblate alignment of the nuclear substates with $\sigma/J = 0.3$.

3.2. The ^{20}Ne nuclei

The two principal transitions of the ^{20}Ne studied by PIGE technique have a pure quadrupolar (E2) multipolarity. Due to the fact that this is an even–even nucleus, its states have an integer spin and, consequently, the gamma-ray angular distribution changes from those obtained for the pure E2 transitions of ^{19}F. Fig. 2(a) and (b) shows the angular distribution of the 1633.602 (15) keV ($j_i^\pi = 2^+ \rightarrow j_f^\pi = 0^+$) and 2613.8 (11) keV ($j_i^\pi = 4^+ \rightarrow j_f^\pi = 2^+$) gamma-rays, respectively. The gain in the gamma-ray intensity to measure the 1633.602 (15) keV gamma-ray at 45° instead of 55° is 13% for total oblate alignment and partial oblate

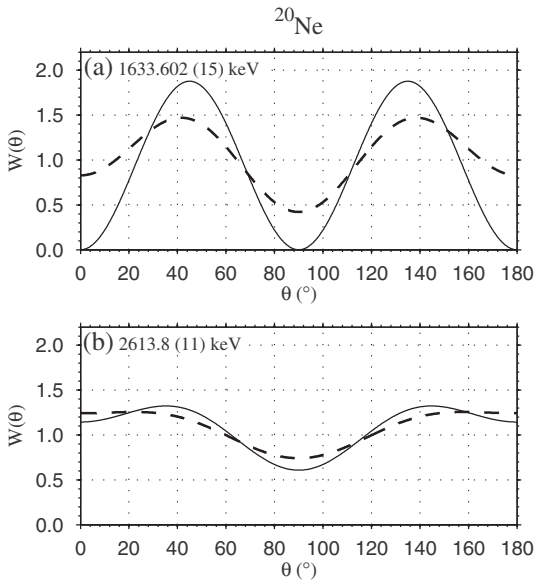

Fig. 2. Angular distribution ($W(\theta)$) of ^{20}Ne gamma-rays: (a) 1633.602 (15) keV and (b) 2613.8 (11) keV. In this figure, the solid line is the angular distribution considering total oblate alignment of the nuclear substates while the dashed line is the angular distribution considering partial oblate alignment of the nuclear substates with $\sigma/J = 0.3$.

alignment of the nuclear substates with $\sigma/J = 0.3$, while for the 2613.8 (11) keV gamma-ray, the gain of the measurement at 35° instead of 55° is 16% for total oblate alignment of the nuclear substates and 19% for partial oblate alignment of the nuclear substates with $\sigma/J = 0.3$ with respect to the measurement at 20°.

3.3. The ^{23}Na nuclei

The first excited state of ^{23}Na has a spin $j_i^\pi = 5/2^+$ and decays to the $j_f^\pi = 3/2^+$ ground state by a 439.986 (10) keV mixed ($\delta = +0.058$ (3)) dipolar (M1) and quadrupolar (E2) transition. As seen in Fig. 3(a), the gain in the gamma-ray intensity to measure the 439.986 (10) keV gamma-ray by changing the detection angle to 90° instead of 55° is 18% for total oblate alignment of the nuclear substates and 16% for partial oblate alignment of the nuclear substates with $\sigma/J = 0.3$. The ^{23}Na 1635.96 (3) keV gamma-ray ($j_i^\pi = 7/2^+ \rightarrow j_f^\pi = 5/2^+$) is also a mixed M1 + E2 transition with mixing ratio $\delta = +0.19$ (1). The angular distribution for this gamma-ray, however is completely different from the angular distribution of the 439.986 (10) keV gamma-ray, as can be seen in Fig. 3(b). In the 1635.96 (3) keV case, the angular distribution is almost isotropic due to the higher mixing ratio and the gain in the gamma-ray intensity is small (7% for total oblate alignment of the nuclear substates and 5% for partial oblate alignment of the nuclear substates with $\sigma/J = 0.3$), by changing the detector angle to 0° instead of 55°. Fig. 3(c) shows the angular distribution of the mixed M1 + E2 627.48 (4) keV gamma-ray ($j_i^\pi = 9/2^+ \rightarrow j_f^\pi = 7/2^+$) and indicates that the gain in the gamma-ray intensity to measure at 90° instead of 55° is 7% for total oblate alignment of the nuclear substates and 5% for partial oblate alignment of the nuclear substates with $\sigma/J = 0.3$.

The experimental data for the ^{23}Na 2263.39 (3) keV gamma-ray [28] ($j_i^\pi = 9/2^+ \rightarrow j_f^\pi = 5/2^+$) indicates that this transition can have a mixed quadrupolar (E2) and dipolar (M3) multipolarity, with mixing ratio $\delta = -0.01$ (3). The angular distribution with this value of δ (see Fig. 3(d)) has a similar shape of a pure E2 transition as the ^{19}F 2582.7 (5) keV gamma-ray (see Fig. 1(d)), but in this case the intensity maximum changes from 45° (pure E2 transition) to 35° (E2 + M3 transition) with total oblate alignment of the nuclear substates and to 20° for partial oblate alignment of the nuclear substates considering $\sigma/J = 0.3$. The gain in the gamma-ray intensity to measure

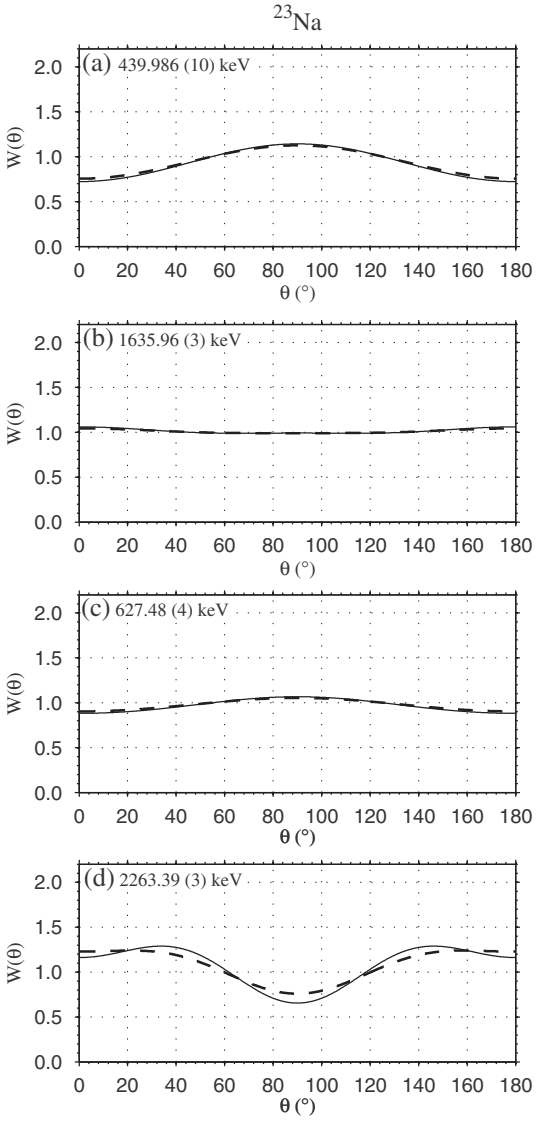

Fig. 3. Angular distribution ($W(\theta)$) of ^{23}Na gamma-rays: (a) 439.986 (10) keV, (b) 1635.96 (3) keV, (c) 627.48 (4) keV and (d) 2263.39 (3) keV. In this figure, the solid line is the angular distribution considering total oblate alignment of the nuclear substates while the dashed line is the angular distribution considering partial oblate alignment of the nuclear substates with $\sigma/J = 0.3$.

at 35° instead of 55° is 16% for total oblate alignment of the nuclear substates and 18% for partial oblate alignment of the nuclear substates with $\sigma/J = 0.3$ measured at 20°.

3.4. The ^{24}Mg nuclei

The two principal transitions of the ^{24}Mg have also a pure quadrupolar (E2) multipolarity and their angular distribution is equal to the ^{20}Ne 1633.602 (15) keV and 2613.8 (11) keV. Fig. 4(a) and (b) shows the angular distribution of the 1368.626 (5) keV ($j_i^\pi = 2^+ \rightarrow j_f^\pi = 0^+$) and 2754.007 (11) keV ($j_i^\pi = 4^+ \rightarrow j_f^\pi = 2^+$) gamma-rays, respectively. The gain in the gamma-ray intensity to measure the 1368.626 (5) keV gamma-ray at 45° instead of 55° is 13% for total oblate alignment of the and partial oblate alignment of the nuclear substates with $\sigma/J = 0.3$, while for the 2754.007 (11) keV gamma-ray, the gain of the measurement at 35° instead of 55° is 16% for total oblate alignment of the nuclear substates and 19% for partial oblate alignment of the nuclear substates with $\sigma/J = 0.3$ with respect to the measurement at 20°.

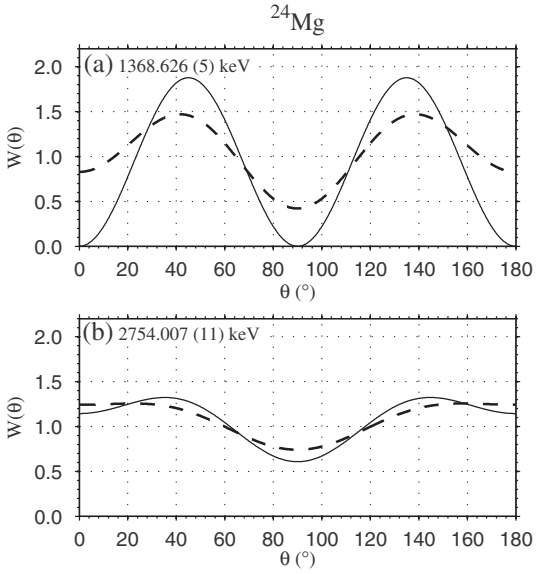

Fig. 4. Angular distribution ($W(\theta)$) of ^{24}Mg gamma-rays: (a) 1368.626 (5) keV and (b) 2754.007 (11) keV. In this figure, the solid line is the angular distribution considering total oblate alignment of the nuclear substates while the dashed line is the angular distribution considering partial oblate alignment of the nuclear substates with $\sigma/J = 0.3$.

3.5. The ^{25}Mg nuclei

The ^{25}Mg 585.028 (30) keV gamma-ray is a quadrupole (E2) transition which decays from $j_i^\pi = 1/2^+$ initial state to a $j_f^\pi = 5/2^+$ final state. Because of the $j_i = 1/2$ initial state, this gamma-ray has also an isotropic distribution (see Fig. 5(a)) as happens to the ^{19}F 109.9 (2) keV gamma-ray. Fig. 5(b) and (c) shows the angular distribution of the mixed M1 + E2 389.710 (35) keV ($\delta = +0.13$ (3)) and 974.742 (35) keV ($\delta = +0.36$ (2)) gamma-rays respectively. In both cases the maximum of the angular distribution is at 90°, resulting in a gain in the gamma-ray intensity for total and partial oblate alignment with $\sigma/J = 0.3$ of 13% for the 389.710 (35) keV gamma-ray and of 25% for the 974.742 (35) keV with respect to the measurement at 55°.

3.6. The ^{26}Mg nuclei

The angular distribution of ^{26}Mg 1808.66 (3) keV ($j_i^\pi = 2^+ \rightarrow j_f^\pi = 0^+$) and 2510.02 (7) keV ($j_i^\pi = 4^+ \rightarrow j_f^\pi = 2^+$) gamma-rays is seen in Fig. 6(a) and (c). Both gamma-rays have a pure quadrupolar (E2) multipolarity and their angular distribution is equal to the ^{24}Mg 1368.626 (5) keV and ^{20}Ne 1633.602 (15) keV ($j_i^\pi = 2^+ \rightarrow j_f^\pi = 0^+$) and to the ^{24}Mg 2754.007 (11) keV and ^{20}Ne 2613.8 (11) keV ($j_i^\pi = 4^+ \rightarrow j_f^\pi = 2^+$) gamma-rays, respectively. So, the gain in the gamma-ray intensity to measure the 1808.66 (3) keV gamma-ray at 45° instead of 55° is 13% for total oblate alignment of the partial oblate alignment of the nuclear substates with $\sigma/J = 0.3$, while for the 2510.02 (7) keV gamma-ray, the gain of the measurement at 35° instead of 55° is 16% for total oblate alignment of the nuclear substates and 19% for partial oblate alignment of the nuclear substates with $\sigma/J = 0.3$ with respect to the measurement at 20°.

Fig. 6(b) shows the angular distribution of the ^{26}Mg 1129.58 (5) keV gamma-ray ($j_i^\pi = 2^+ \rightarrow j_f^\pi = 2^+$), a mixed dipolar (M1) and quadrupolar (E2) multipolarity with mixing ratio $\delta = -0.12$ (2). The gain in the gamma-ray intensity to measure this gamma-ray by changing the detection angle to 0° instead of 55° is 31% for total oblate alignment of the nuclear substates and 26% for partial oblate alignment of the nuclear substates with $\sigma/J = 0.3$.

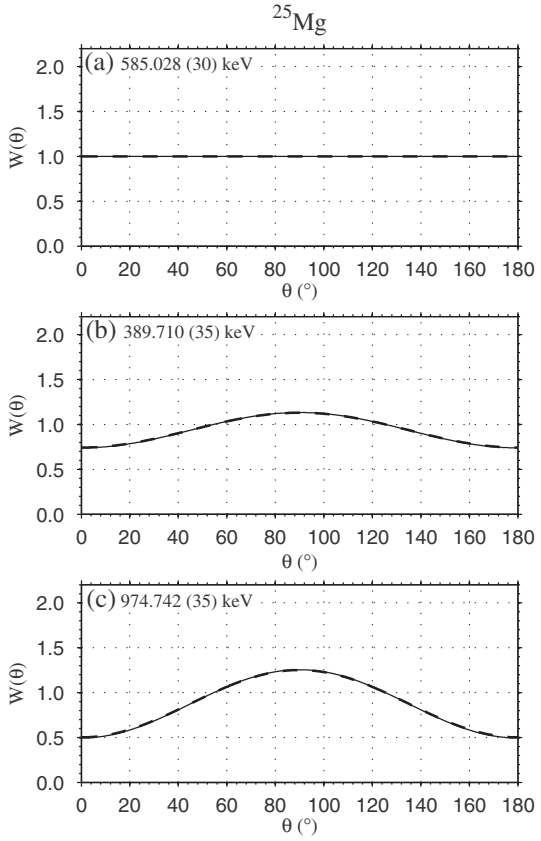

Fig. 5. Angular distribution ($W(\theta)$) of ^{25}Mg gamma-rays: (a) 585.028 (30) keV, (b) 389.710 (35) keV and (c) 974.742 (35) keV. In this figure, the solid line is the angular distribution considering total oblate alignment of the nuclear substates while the dashed line is the angular distribution considering partial oblate alignment of the nuclear substates with $\sigma/J = 0.3$.

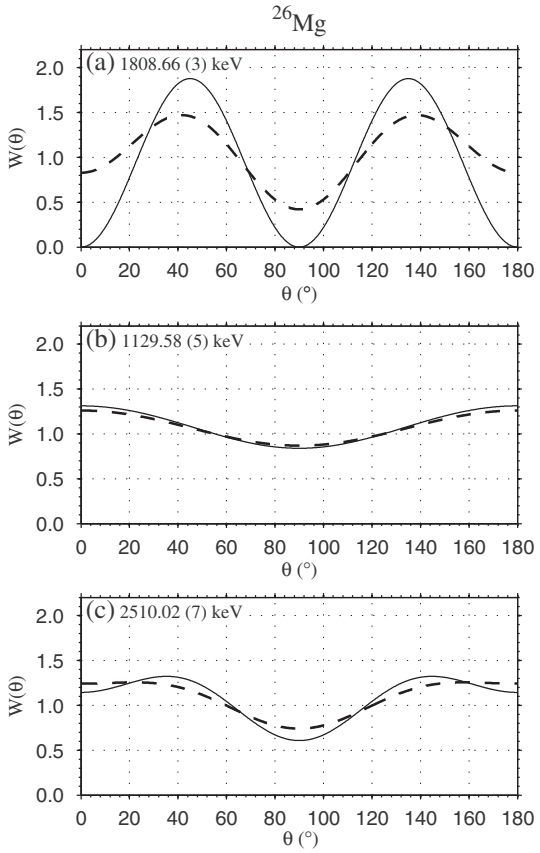

Fig. 6. Angular distribution ($W(\theta)$) of ^{26}Mg gamma-rays: (a) 1808.66 (3) keV, (b) 1129.58 (5) keV and (c) 2510.02 (7) keV. In this figure, the solid line is the angular distribution considering total oblate alignment of the nuclear substates while the dashed line is the angular distribution considering partial oblate alignment of the nuclear substates with $\sigma/J = 0.3$.

3.7. The ^{27}Al nuclei

In Fig. 7(a), the angular distribution of the ^{27}Al 843.76 (10) keV gamma-ray ($j_i^\pi = 1/2^+ \rightarrow j_f^\pi = 5/2^+$) is shown. This gamma-ray has also an isotropic distribution due to the $j_i = 1/2$ initial state, as happens to the ^{25}Mg 585.028 (30) keV and ^{19}F 109.9 (2) keV transitions.

Fig. 7(b) and (c) shows the angular distribution of the mixed M1 + E2 ^{27}Al 1014.52 (10) keV ($\delta = -0.351$ (12)) and 2212.01 (10) keV ($\delta = +0.468$ (9)) gamma-rays. The gain in the gamma-ray intensity to measure this gamma-ray by changing the detection angle to 0° instead of 55° for the 1014.52 (10) keV is 24% for total and partial oblate alignment of the nuclear substates with $\sigma/J = 0.3$, while for the 2212.01 (10) keV it is 70% for total oblate alignment of the nuclear substates and 53% for partial oblate alignment of the nuclear substates with $\sigma/J = 0.3$.

3.8. The ^{28}Si nuclei

The ^{28}Si 1778.969 (11) keV gamma-ray ($j_i^\pi = 2^+ \rightarrow j_f^\pi = 0^+$) has the same angular distribution of the ^{26}Mg 1808.66 (3) keV, ^{24}Mg 1368.626 (5) keV and ^{20}Ne 1633.602 (15) keV transitions, as can be seen in Fig. 8(a). The same happens to the ^{28}Si 2838.29 (15) keV gamma-ray ($j_i^\pi = 4^+ \rightarrow j_f^\pi = 2^+$), which also has an angular distribution similar to the ^{26}Mg 2510.02 (7) keV, ^{24}Mg 2754.007 (11) keV and ^{20}Ne 2613.8 (11) keV gamma-rays. The gain in the gamma-ray intensity to measure the ^{28}Si 1778.969 (11) keV gamma-ray at 45° instead of 55° is 13% for total oblate alignment of the and partial oblate alignment of the nuclear substates with $\sigma/J = 0.3$, while for the 2838.29 (15) keV gamma-ray, the gain of the measurement at 35° instead of 55° is 16% for total oblate alignment of the nuclear substates and 19% for partial oblate alignment of the nuclear substates with $\sigma/J = 0.3$ with respect to the measurement at 20°.

3.9. The ^{29}Si nuclei

In Fig. 9(a) and (b) the angular distribution of the ^{29}Si mixed M1 + E2 1273.361 (9) keV ($\delta = +0.197$ (9)) and 1793.83 (8) keV ($\delta = +0.26$ (2)) gamma-rays is shown. The gain in the gamma-ray intensity to measure the 1273.361 (9) keV gamma-ray by changing the detection angle to 90° instead of 55° for the 1273.361 (9) keV is only 6% for total and partial oblate alignment of the nuclear substates with $\sigma/J = 0.3$, while for the 1793.83 (8) keV it is 19% for total oblate alignment of the nuclear substates and 15% for partial oblate alignment of the nuclear substates with $\sigma/J = 0.3$ to measure at 0° instead of measuring at 55°.

3.10. The ^{30}Si nuclei

The ^{30}Si 2235.23 (2) keV and 3498.33 (5) keV gamma-rays ($j_i^\pi = 2^+ \rightarrow j_f^\pi = 0^+$) are pure quadrupolar (E2) transitions and have the same angular distributions of the ^{28}Si 1778.969 (11) keV, ^{26}Mg 1808.66 (3) keV, ^{24}Mg 1368.626 (5) keV and ^{20}Ne 1633.602 (15) keV transitions, as can be seen in Fig. 10(a) and (c). The same happens to the ^{30}Si 3043.2 (1) keV gamma-ray ($j_i^\pi = 4^+ \rightarrow j_f^\pi = 2^+$), which also has an angular distribution (see Fig. 10(a)) equal to the ^{28}Si 2838.29 (15) keV, ^{26}Mg 2510.02 (7) keV, ^{24}Mg 2754.007 (11) keV and ^{20}Ne 2613.8 (11) keV gamma-rays. The gain in the gamma-ray intensity to measure the ^{30}Si 2235.23 (2) keV and 3498.33 (5) keV gamma-rays at

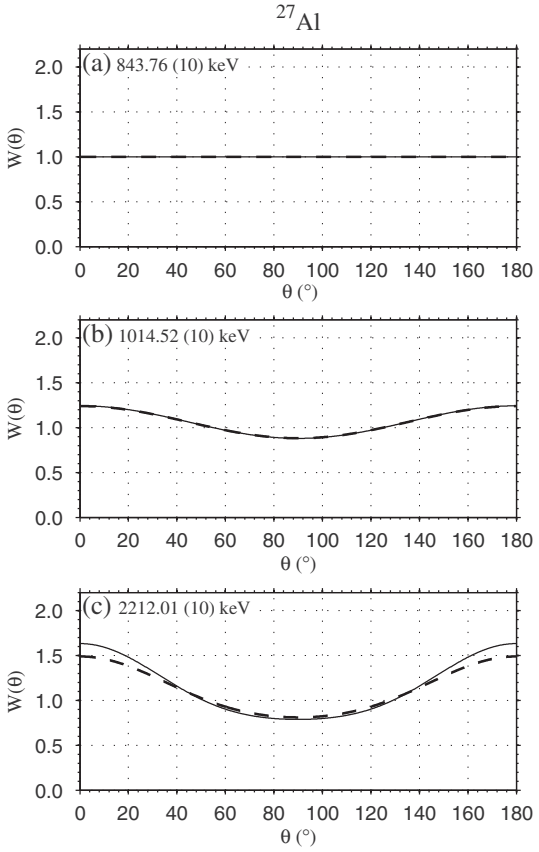

Fig. 7. Angular distribution ($W(\theta)$) of ^{27}Al gamma-rays: (a) 843.76 (10) keV, (b) 1014.52 (10) keV and (c) 2212.01 (10) keV. In this figure, the solid line is the angular distribution considering total oblate alignment of the nuclear substates while the dashed line is the angular distribution considering partial oblate alignment of the nuclear substates with $\sigma/J = 0.3$.

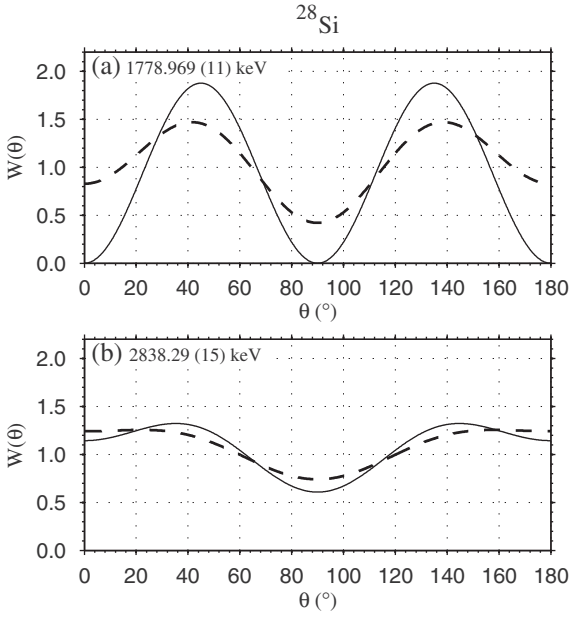

Fig. 8. Angular distribution ($W(\theta)$) of ^{28}Si gamma-rays: (a) 1778.969 (11) keV and (b) 2838.29 (15) keV. In this figure, the solid line is the angular distribution considering total oblate alignment of the nuclear substates while the dashed line is the angular distribution considering partial oblate alignment of the nuclear substates with $\sigma/J = 0.3$.

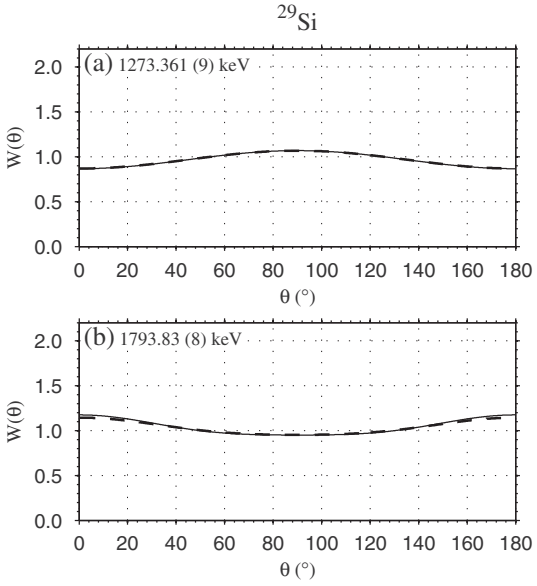

Fig. 9. Angular distribution ($W(\theta)$) of ^{29}Si gamma-rays: (a) 1273.361 (9) and (b) 1793.83 (8). In this figure, the solid line is the angular distribution considering total oblate alignment of the nuclear substates while the dashed line is the angular distribution considering partial oblate alignment of the nuclear substates with $\sigma/J = 0.3$.

45° instead of 55° is 13% for total oblate alignment of the and partial oblate alignment of the nuclear substates with $\sigma/J = 0.3$, while for the 3043.2 (1) keV gamma-ray, the gain o measure at 35° instead of 55° is 16% for total oblate alignment of the nuclear substates and 18.5% for partial oblate alignment of the nuclear substates with $\sigma/J = 0.3$ with respect to the measurement at 20°.

Fig. 10(b) shows the angular distribution of the ^{30}Si 1263.13 (3) keV gamma-ray ($j_i^\pi = 2^+ \rightarrow j_f^\pi = 2^+$), a mixed dipolar (M1) and quadrupolar (E2) multipolarity with mixing ratio $\delta = +0.18$ (5). In this case, the gain in the gamma-ray intensity to measure this gamma-ray by changing the detection angle to 0° instead of 55° is 72% for total oblate alignment of the nuclear substate and 60% for partial oblate alignment of the nuclear substates with $\sigma/J = 0.3$.

3.11. The ^{31}P nuclei

The angular distribution (see Fig. 11(a)) of the mixed M1 + E2 ^{31}P 1266.1 (1) keV gamma-ray ($\delta = +0.28$ (2)) is similar to the ^{23}Na 1635.96 (3) keV gamma-ray. The angular distribution is almost isotropic due to the higher mixing ratio and the gain in the gamma-ray intensity is very small (2% for total and partial oblate alignment of the nuclear substates with $\sigma/J = 0.3$) by changing the detector angle to 0° instead of 55°.

Fig. 11(b) shows the angular distribution of the ^{31}P 2028.8 (2) keV gamma-ray ($j_i^\pi = 5/2^+ \rightarrow j_f^\pi = 3/2^+$), a mixed dipolar (M1) and quadrupolar (E2) multipolarity with mixing ratio $\delta = +0.44$ (2). In this case, the gain in the gamma-ray intensity to measure this gamma-ray by changing the detection angle from 55° to 0° is 62% for total oblate alignment of the nuclear substate and 50% for partial oblate alignment of the nuclear substates with $\sigma/J = 0.3$.

3.12. Summary of the results

Table 2 summarizes the new suggested detector position angle related to the beam direction and the gain in intensity compared with the standard detector position (55° or 125°) calculated for the gamma-rays of ^{19}F, ^{20}Ne, ^{23}Na, ^{24,25,26}Mg, ^{27}Al, ^{28,29,30}Si and ^{31}P nuclei.

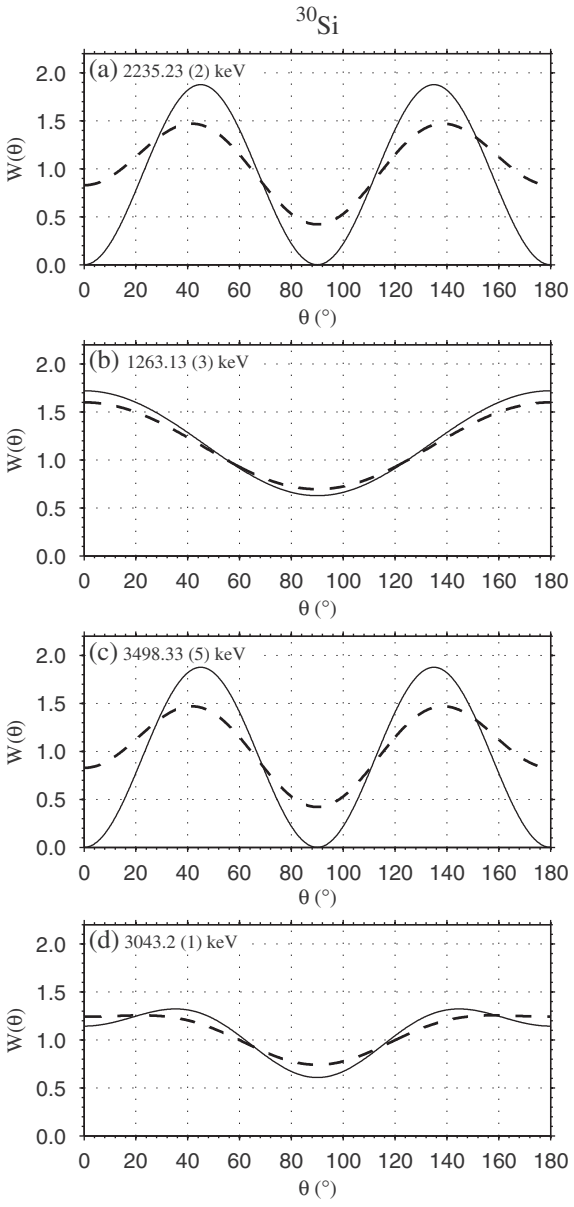

Fig. 10. Angular distribution ($W(\theta)$) of ^{30}Si gamma-rays: (a) 1263.13 (3) keV, (b) 2235.23 (2) keV, (c) 3498.33 (5) and (d). In this figure, the solid line is the angular distribution considering total oblate alignment of the nuclear substates while the dashed line is the angular distribution considering partial oblate alignment of the nuclear substates with $\sigma/J = 0.3$.

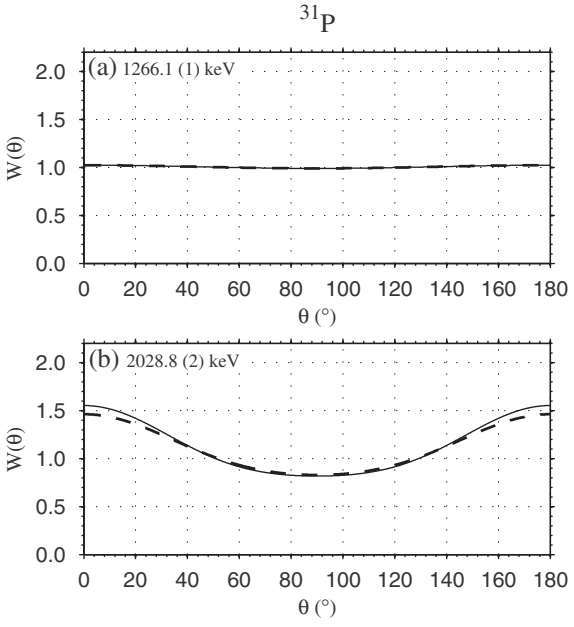

Fig. 11. Angular distribution ($W(\theta)$) of ^{31}P gamma-rays: (a) 1266.1 (1) keV and (b) 2028.8 (2) keV. In this figure, the solid line is the angular distribution considering total oblate alignment of the nuclear substates while the dashed line is the angular distribution considering partial oblate alignment of the nuclear substates with $\sigma/J = 0.3$.

4. Conclusions

In this work gamma-ray angular distributions of some of the widely studied isotopes applying the PIGE technique were calculated to determine the optimum position of the gamma-ray detector in order to maximize the gamma-ray detection efficiency and minimize the applied radiation dose to the studied object.

It was observed that the angular distribution is symmetric with respect to 90° and depends on the initial and final state spins and on the transition multipolarity. Pure E2 multipolarity angular distribution shows maxima at 45° or 135° and minima at 0°, 90° and 180°. The intensity of the maxima and the minima can change depending whether the initial and final states have an integer or a half-integer spin. Mixed M1 + E2 transitions can have different angular distributions where maxima and minima angles occur due to the dependency on the degree of the mixture, given by the mixing ratio δ and the initial state spin.

Table 2
New detector position angle suggested considering total oblate alignment of the nuclear substates m for the gamma-rays of the measured ^{19}F, ^{20}Ne, ^{23}Na, ^{24,25,26}Mg, ^{27}Al, ^{28,29,30}Si and ^{31}P nuclei. The calculated gain in intensity compared with the standard detector position (55° or 125°) is also shown. The columns labeled E_γ, j_i and j_f made reference to the gamma-ray energies (in keV) and the initial and final state spins of the nuclear states, respectively.

Measured nuclei	E_γ (keV)	j_i	j_f	Suggested detector position angle (total alignment)	Intensity improvement (%)
^{19}F	109.9 (2)	$1/2^-$	$1/2^+$	All	0
	197.1 (2)	$5/2^+$	$1/2^+$	45° or 135°	13
	1235.8 (5)	$5/2^-$	$1/2^-$	45° or 135°	13
	2582.7 (5)	$9/2^+$	$5/2^+$	45° or 135°	12
^{20}Ne	1633.602 (15)	2^+	0^+	45° or 135°	13
	2613.8 (11)	4^+	2^+	45° or 135°	16
^{23}Na	439.986 (10)	$5/2^+$	$3/2^+$	90°	18
	1635.96 (3)	$7/2^+$	$5/2^+$	0° or 180°	7
	627.48 (4)	$9/2^+$	$7/2^+$	90°	7
	2263.39 (3)	$9/2^+$	$5/2^+$	35°	16
^{24}Mg	1368.626 (5)	2^+	0^+	45° or 135°	13
	2754.007 (11)	4^+	2^+	45° or 135°	16
^{25}Mg	585.028 (30)	$1/2^+$	$5/2^+$	All	0
	389.710 (35)	$1/2^+$	$3/2^+$	90°	13
	974.742 (35)	$3/2^+$	$5/2^+$	90°	25
^{26}Mg	1808.66 (3)	2^+	0^+	45° or 135°	13
	1129.58 (5)	2^+	2^+	0° or 180°	31
	2510.02 (7)	4^+	2^+	45° or 135°	16
^{27}Al	843.76 (10)	$1/2^+$	$5/2^+$	All	0
	1014.52 (10)	$3/2^+$	$5/2^+$	0° or 180°	24
	2212.01 (10)	$(7/2^+)$	$5/2^+$	0° or 180°	70
^{28}Si	1778.969 (11)	2^+	0^+	45° or 135°	13
	838.29 (15)	$3/2^+$	$5/2^+$	45° or 135°	16
^{29}Si	1273.361 (9)	$3/2^+$	$1/2^+$	90°	6
	1793.83 (8)	$5/2^+$	$3/2^+$	0° or 180°	19
^{30}Si	1263.13 (3)	2^+	2^+	0° or 180°	72
	2235.23 (2)	2^+	0^+	5° or 135°	13
	3498.33 (5)	2^+	0^+	5° or 135°	13
	3043.2 (1)	4^+	2^+	45° or 135°	16
^{31}P	1266.1 (1)	$3/2^+$	$1/2^+$	0° or 180°	2
	2028.8 (2)	$5/2^+$	$3/2^+$	0° or 180°	62

The best position of the gamma-ray detector considering the angular distribution of a pure E2 state, such as the first transitions of the ^{20}Ne (1633.602 (15) keV gamma-ray), ^{24}Mg (1368.626 (5) keV), ^{28}Si (1778.969 (11) keV) and ^{30}Si (2235.23 (2) keV) is 45° and 135° with respect to the beam direction. In this case, the gain in the gamma-ray intensity can be up to 19% (depending on the occurrence of a completely alignment or not) if the detector is placed at the maxima of the gamma-ray angular distribution instead of the standard detector position (55° or 125°).

For a mixed M1 + E2 transition, the best position of the gamma-ray detector considering the angular distribution varies from 0° to 90°, depending on the initial state spin and the value of the mixing ratio δ. However, if the detector is placed in the maxima of the mixed angular distribution, the gain in the gamma-ray intensity can be up to 70% compared to the standard detector position.

The calculations are promising and represent an alternative to analyze elemental material samples by using the PIGE technique in the cases where a specific element is under study by changing the detector angle position due to the previous knowledge of the gamma-ray angular distributions in order to maximize the gamma-ray detection efficiency and to minimize the applied radiation dose to the object under study.

Acknowledgments

This work was supported by grant 2013/19976-8, São Paulo Research Foundation (FAPESP), Brazil.

References

[1] M.J. Kenny, J.R. Bird, E. Clayton, Proton induced γ-ray yields, Nucl. Inst. Methods 168 (1980) 115–120, http://dx.doi.org/10.1016/0029-554X(80)91240-9.
[2] A. Anttila, R. Hänninen, J. Räisänen, Proton-induced thick-target gamma-ray yields for the elemental analysis of the Z = 3–9, 11–21 elements, J. Radioanal. Chem. 62 (1981) 293–306, http://dx.doi.org/10.1007/BF02517360.
[3] G. Ezeh, I. Obioh, O. Asubiojo, M. Chiari, S. Nava, G. Calzolai, F. Lucarelli, C. Nuviadenu, The complementarity of PIXE and PIGE techniques: a case study of size segregated airborne particulates collected from a Nigeria city, Appl. Radiat. Isot. 103 (2015) 82–92, http://dx.doi.org/10.1016/j.apradiso.2015.05.015.
[4] H. Yamamoto, Y. Iwami, K. Yagi, M. Hayashi, H. Komatsu, K. Okuyama, Y. Matsuda, K. Yasuda, Evaluation of caries progression in dentin treated by fluoride-containing materials using an in-air micro-PIGE and micro-PIXE measurement system, Nucl. Inst. Methods Phys. Res. B: Beam Interact. Mater. Atoms 348 (2015) 152–155, http://dx.doi.org/10.1016/j.nimb.2015.01.068.
[5] R.K. Bhanisana Devi, H.N. Sarma, S. Kumar, Investigation on trace and major elements in anti-asthmatic medicinal plants by PIXE and PIGE techniques, Nucl. Inst. Methods Phys. Res. B: Beam Interact. Mater. Atoms 343 (2015) 163–166, http://dx.doi.org/10.1016/j.nimb.2014.11.077.
[6] L. Csedreki, R. Huszank, Application of PIGE, BS and NRA techniques to oxygen profiling in steel joints using deuteron beam, Nucl. Inst. Methods Phys. Res. B: Beam Interact. Mater. Atoms 348 (2015) 165–169, http://dx.doi.org/10.1016/j.nimb.2014.12.013.
[7] T. Calligaro, J.-C. Dran, J.-P. Poirot, G. Querr, J. Salomon, J. Zwaan, PIXE/PIGE characterisation of emeralds using an external micro-beam, Nucl. Inst. Methods Phys. Res. B: Beam Interact. Mater. Atoms 161163 (2000) 769–774, http://dx.doi.org/10.1016/S0168-583X(99)00974-X.
[8] K. Dasari, S. Chhillar, R. Acharya, D. Ray, A. Behera, N. Lakshmana Das, P. Pujari, Simultaneous determination of Si, Al and Na concentrations by particle induced gamma-ray emission and applications to reference materials and ceramic archaeological artifacts, Nucl. Inst. Methods Phys. Res. B: Beam Interact. Mater. Atoms 339 (2014) 37–41, http://dx.doi.org/10.1016/j.nimb.2014.08.017.
[9] Z. Šmit, T. Milavec, H. Fajfar, T. Rehren, J.W. Lankton, B. Gratuze, Analysis of glass from the post-Roman settlement Tonovcov grad (Slovenia) by PIXE-PIGE and LA-ICP-MS, Nucl. Inst. Methods Phys. Res. B: Beam Interact. Mater. Atoms 311 (2013) 53–59, http://dx.doi.org/10.1016/j.nimb.2013.06.012.
[10] N. Grassi, A. Migliori, P. Mandò, H. Calvo Del Castillo, Identification of lapis-lazuli pigments in paint layers by PIGE measurements, Nucl. Inst. Methods Phys. Res. B: Beam Interact. Mater. Atoms 219–220 (2004) 48–52, http://dx.doi.org/10.1016/j.nimb.2004.01.026.
[11] T. Calligaro, J.-C. Dran, J. Salomon, Ion beam microanalysis, in: K. Janssens, R. Van Grieken (Eds.), Non-destructive microanalysis of Cultural Heritage materials, vol. 42 of Comprehensive Analytical Chemistry, Elsevier, 2004, (Ch. 5), pp. 227–276. doi:http://dx.doi.org/10.1016/S0166-526X(04)80009-6.
[12] F. Lucarelli, G. Calzolai, M. Chiari, M. Giannoni, D. Mochi, S. Nava, L. Carraresi, The upgraded external-beam pixe/pige set-up at LABEC for very fast measurements on aerosol samples, Nucl. Inst. Methods Phys. Res. B: Beam Interact. Mater. Atoms 318 (Part A) (2014) 55–59, http://dx.doi.org/10.1016/j.nimb.2013.05.099.
[13] I. Rajta, I. Borbély-Kiss, G. Mórik, L. Bartha, E. Koltay, Á.Z. Kiss, The new ATOMKI scanning proton microprobe, Nucl. Inst. Methods Phys. Res. B: Beam Interact. Mater. Atoms 109110 (1996) 148–153, http://dx.doi.org/10.1016/0168-583X(95)00897-7.
[14] J. Salomon, J.-C. Dran, T. Guillou, B. Moignard, L. Pichon, P. Walter, F. Mathis, Present and future role of ion beam analysis in the study of Cultural Heritage materials: the example of the {AGLAE} facility, Nucl. Inst. Methods Phys. Res. B: Beam Interact. Mater. Atoms 266 (2008) 2273–2278, http://dx.doi.org/10.1016/j.nimb.2008.03.076.
[15] L. Beck, P.C. Gutiérrez, F. Miserque, L. Thomé, Proton beam modification of lead white pigments, Nucl. Inst. Methods Phys. Res. B: Beam Interact. Mater. Atoms 307 (2013) 20–24, http://dx.doi.org/10.1016/j.nimb.2012.12.073.
[16] O. Enguita, T. Calderón, M.T. Fernández-Jiménez, P. Beneitez, A. Millan, G. Garca, Damage induced by proton irradiation in carbonate based natural painting pigments, Nucl. Inst. Methods Phys. Res. B: Beam Interact. Mater. Atoms 219–220 (2004) 53–56, http://dx.doi.org/10.1016/j.nimb.2004.01.027.
[17] J. Absil, H.P. Garnir, D. Strivay, C. Oger, G. Weber, Study of color centers induced by PIXE irradiation, Nucl. Inst. Methods Phys. Res. B: Beam Interact. Mater. Atoms 198 (2002) 90–97, http://dx.doi.org/10.1016/S0168-583X(02)01522-7.
[18] M. Chiari, A. Migliori, P.A. Mandò, Investigation of beam-induced damage to ancient ceramics in external-PIXE measurements, Nucl. Inst. Methods Phys. Res. B: Beam Interact. Mater. Atoms 188 (2002) 151–155, http://dx.doi.org/10.1016/S0168-583X(01)01065-5.
[19] H. Morinaga, T. Yamazaki, In-beam Gamma-ray Spectroscopy, North-Holland Pub. Co., 1976
[20] J.-P. Hirnoven, Nuclear reaction analysis: particle-gamma reactions, in: J. Tesmer, M. Nastasi (Eds.),Handbook of Modern Ion Beam Materials Analysis, Materials Research Society 1995, p. 174.
[21] K.S. Krane, R.M. Steffen, Determination of the E2/M1 multipole mixing ratios of the gamma transitions in Cd^{110}, Phys. Rev. C 2 (1970) 724–734, http://dx.doi.org/10.1103/PhysRevC.2.724.
[22] Nuclear data sheets symbols and abbreviations, Nucl. Data Sheets 124 (2015)http://dx.doi.org/10.1016/S0090-3752(14)00752-2 (IBC –).
[23] A.E. Stuchbery, γ-Ray angular distributions and correlations after projectile-fragmentation reactions, Nucl. Phys. A 723 (2003) 69–92, http://dx.doi.org/10.1016/S0375-9474(03)01157-6.
[24] A. Fergunson, Angular correlation methods in gamma-ray spectroscopy, North-Holland Pub. Co., 1965.
[25] The Math Works Inc., MATLAB 8.1 (R2013a), The Math Works Inc., 2013
[26] M. Berglund, M.E. Wieser, Isotopic compositions of the elements 2009 (IUPAC technical report), Pure Appl. Chem. 83 (2011) 397–410, http://dx.doi.org/10.1351/PAC-REP-10-06-02.
[27] D. Tilley, H. Weller, C. Cheves, R. Chasteler, Energy levels of light nuclei A = 18–19, Nucl. Phys. A 595 (1995) 1–170, http://dx.doi.org/10.1016/0375-9474(95)00338-1.
[28] R. Firestone, Nuclear data sheets for A = 23, Nucl. Data Sheets 108 (2007) 1–78, http://dx.doi.org/10.1016/j.nds.2007.01.002.
[29] R. Firestone, Nuclear data sheets for A = 24, Nucl. Data Sheets 108 (2007) 2319–2392, http://dx.doi.org/10.1016/j.nds.2007.10.001.
[30] D. Tilley, C. Cheves, J. Kelley, S. Raman, H. Weller, Energy levels of light nuclei, A = 20, Nucl. Phys. A 636 (1998) 249–364, http://dx.doi.org/10.1016/S0375-9474(98)00129-8.
[31] R. Firestone, Nuclear data sheets for A = 25, Nucl. Data Sheets 110 (2009) 1691–1744, http://dx.doi.org/10.1016/j.nds.2009.06.001.
[32] P. Endt, Supplement to energy levels of A = 2144 nuclei (VII), Nucl. Phys. A 633 (1998) 1–220, http://dx.doi.org/10.1016/S0375-9474(97)00613-1.
[33] M. Shamsuzzoha Basunia, Nuclear data sheets for A = 27, Nucl. Data Sheets 112 (2011) 1875–1948, http://dx.doi.org/10.1016/j.nds.2011.08.001.
[34] M. Shamsuzzoha Basunia, Nuclear data sheets for A = 28, Nucl. Data Sheets 114 (2013) 1189–1291, http://dx.doi.org/10.1016/j.nds.2013.10.001.
[35] M. Shamsuzzoha Basunia, Nuclear data sheets for A = 29, Nucl. Data Sheets 113 (2012) 909–972, http://dx.doi.org/10.1016/j.nds.2012.04.001.
[36] M. Shamsuzzoha Basunia, Nuclear data sheets for A = 30, Nucl. Data Sheets 111 (2010) 2331–2424, http://dx.doi.org/10.1016/j.nds.2010.09.001.
[37] C. Ouellet, B. Singh, Nuclear data sheets for A = 31, Nucl. Data Sheets 114 (2013) 209–396, http://dx.doi.org/10.1016/j.nds.2013.03.001.